A Near-Field Dual Polarized (TE–TM) Microwave Imaging System

Majid Ostadrahimi, *Member, IEEE*, Amer Zakaria, *Member, IEEE*, Joe LoVetri, *Senior Member, IEEE*, and Lotfollah Shafai, *Life Fellow, IEEE*

Abstract—In this paper, we introduce a novel dual polarized microwave imaging system. The system is comprised of a circular array of multiplexed antennas, distributed evenly around an object-of-interest (OI), along with a novel plurality of probes located at the antennas' apertures. Each probe consists of several p-i-n diodes biased in two different states (open and short). The probes are used to measure field scattered by an OI based on the modulated scatterer technique. Half of the probes are oriented vertically with the second half oriented horizontally. The presence of the two probe-orientations enables the imaging system to collect two orthogonal field polarizations, transverse electric (TE) and transverse magnetic (TM), without the need for mechanical rotation. In order to illuminate the object with all possible polarizations of the electromagnetic field, the transmitting antennas are placed at a slant angle with respect to the longitudinal plane of the imaging chamber. Near-field data are collected using each probe set, then calibrated. We show that the calibrated data for each polarization can be used to reconstruct the dielectric profile of various objects using either two-dimensional TE or TM inversion algorithms.

Index Terms—Microwave imaging (MWI), microwave tomography, modulated scatterer technique (MST), transverse electric (TE) polarization, transverse magnetic (TM) polarization.

I. INTRODUCTION

MICROWAVE IMAGING (MWI) has been deployed in many industrial, biomedical, and security applications such as nondestructive testing and evaluation [1], geophysical surveying [2], and breast cancer diagnostics [3].

An MWI system may consist of only a single transmitter/receiver antenna [4] or a multiplexed array of antennas [5], which may be repositioned for generating more data. The basic operation of the system is based on illuminating an object-of-interest (OI) by a transmitting antenna, and collecting the scattered fields at various receiving locations. The collected field data are calibrated and then processed using nonlinear inverse scattering algorithms [6]–[9] or radar techniques [10]. Depending on the application, the outcome is either a *quantitative* reconstruction of the complex dielectric profile of the OI that also provides information on its shape and location, or a *qualitative* image

that produces the *shadow* of the OI. The latter method does not incur the heavy computational burden of quantitative MWI and can be accomplished in real time [1]; nevertheless, qualitative imaging cannot provide information about the internal structure and composition of the OI, as in quantitative MWI, which is a necessity in biomedical and geo-surveying applications.

In order to obtain a quantitative *interior* image of an OI, the microwave energy should penetrate sufficiently into the object. To reduce reflections from the boundary of the OI, thus maximizing field penetration, it is typically immersed into a matching fluid [11], [12]. Furthermore, because wave penetration depth is inversely proportional to the frequency of operation, there are upper limits on the frequency that can be used, especially when imaging biologicial targets. Typically, MWI systems for biomedical applications operate up to C-band, e.g., 915 MHz [13], 1.0–2.3 GHz [14], 2.45 GHz [11], or 0.9–1.5 GHz [15].

Due to the low operational frequency and the compact size of these systems, the target is located in the near-field region of the antennas. In this region, complicated field distributions will exist due to the presence of some or all polarizations, arbitrary wave impedances, and both propagating, as well as evanescent, modes. Note that polarization is a unique aspect of MWI, not usually available in most other imaging modalities, which can be exploited as a source of information.

The proper use of different polarizations requires: 1) inversion algorithms capable of inverting vector field problems; 2) specialized measurement techniques sensitive to individual polarizations; and 3) proper calibration techniques. The ability to use arbitrary polarizations of electromagnetic energy requires full-wave computational models of the imaging chamber, otherwise modeling error increases, making imaging difficult [16]. Such full-wave modeling of the imaging system is computationally expensive. Further, the measurement of different polarizations requires sophisticated experimental systems that can differentiate between measured signal polarizations. Furthermore, the associated calibration techniques have to be tailored for each polarization and for the specific measurement system being used. Existing imaging systems either measure only a single field polarization in the near-field region [6], [14], [17], or place the antennas in the far-field region and rotate the antennas to collect two field polarizations, e.g., see [4] and [18].

Although near-field transverse electric (TE)–transverse magnetic (TM) systems have been reported in the past for microwave reflectometer applications, where two orthogonal polarizations are excited by switching the feed locations of the antenna [19], to the authors' knowledge there are no experimental near-field MWI systems that collect the TE mode

electric fields that are located solely in the near-field transverse plane of the system. The 2-D imaging system described herein can simultaneously collect both the TE and TM polarization in the near-field region.

In this paper, the system is implemented using the modulated scatterer technique (MST) [20] that we refer to as an indirect field measurement approach. In this approach, the field is collected using some scattering probes, which are modulated using several p-i-n diodes per probe [21]. It is an extension of a previously implemented 2-D TM MST-based tomography system [21]. For the 2-D TM case, it was shown how one could increase the number of probing sites while reducing the number of collector antennas [22]. For the present dual polarized system, we utilize new cavity-backed Vivaldi antennas, as transmitters and collectors, positioned at a slant angle with respect to the longitudinal plane of the chamber. The use of the conducting cavity in the antennas provides shielding from the diode-biasing wires, thus making their effect on the field within the chamber negligible. Such effects, if nonnegligible, would need to be taken into account in the imaging algorithms [21].

The collected data are calibrated separately for each polarization, then are used to reconstruct the 2-D complex permittivity profiles for several OIs. The calibration procedure along with the algorithm utilized to invert the data are outlined in this paper.

This paper is organized as follows. The imaging system is described in Section II, followed by a description of the calibration techniques used for both the TM and TE polarizations in Section III. To study the imaging performance of the system, four dielectric phantoms are utilized whose images are provided in Sections IV and V. Finally, we comment on the performance of using each polarization for imaging and we provide some future directions of research.

II. System Description

We have previously designed and implemented an MST-based imaging system that only collects the TM-polarized fields. The full-description of the 2-D TM MST system is outlined in [21]. Similar to the single-polarized system, the dual-polarized system consists of a vector network analyzer (VNA), an RF switch multiplexer, a driver circuit for controlling the probes, antennas that are distributed evenly around the measurement chamber, and the probes. A photograph and schematic representation of the system are shown in Fig. 1(a) and (b), respectively. In this section, the operation of the system is described.

A. Data Acquisition

The OI is successively illuminated by the antennas. For each object, two sets of measurements are required: a measurement with the presence of the object inside the chamber that is referred to as the $\vec{E}^{\text{tot}}$ or the total-field measurement, and a measurement with the absence of the object that is referred to as the $\vec{E}^{\text{inc}}$ or the incident-field measurement. Subtracting the $\vec{E}^{\text{inc}}$ from the $\vec{E}^{\text{tot}}$ results in the scattered field data required by the imaging algorithm.
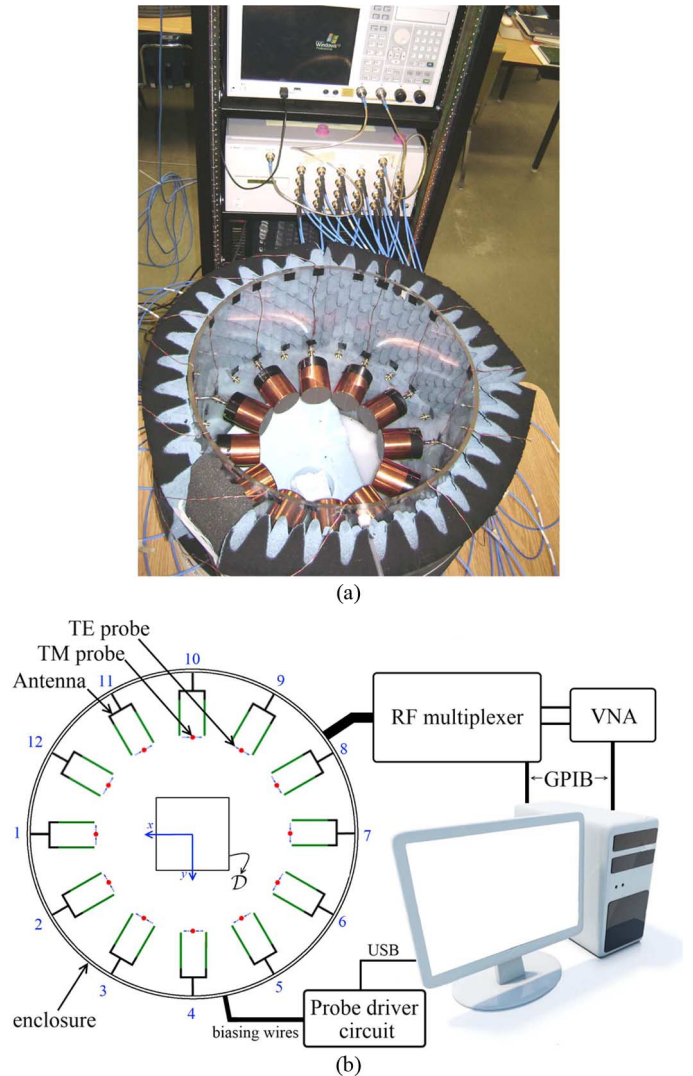

Fig. 1. (a) Photograph of the dual-polarized imaging system. (b) Schematic representation of the system including the imaging domain $\mathcal{D}$ location.

B. MST-Based Differential S-Parameter Measurement

A traditional MST system, originally introduced in the 1950s [23], consists of a probe (e.g., a dipole wire [17], [21], [24] or an elliptical slot [25]) and a collector antenna. In [1], [11], and [17], a single collector antenna is utilized and is located in close proximity to an array of scattering probes; this system configuration is referred to as a retina. In order to measure the field at the probe's location, the probe is modulated with a very low frequency signal, which can be differentiated from the frequency of the field to be measured. The modulation can be mechanical [26], optical [24], or electrical [25].

The MST is based on the fact that the field scattered by the probe is proportional to the original field at the probe's location. The collector antenna thus collects a modulated signal that is proportional to the field *only* at the probe's location [20].

In our system, each probe is a printed wire dipole, equipped with five p-i-n diodes in series, distributed along the probe's length. The length and width of each probe are 42.8 and 0.5 mm, respectively. Further, each probe interacts with a field polarization parallel to its axis. The use of 5 p-i-n diodes improves the probe's performance [21]. The multiplexed array enables our
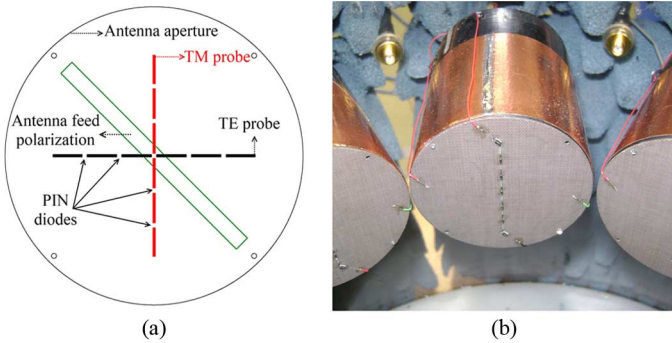
Fig. 2. (a) Configuration of the TE and TM probes. (b) Photograph of the antenna including the probes at the aperture.

imaging system to switch the transmitter antenna, as well as the collector antennas, successively to collect data at different points surrounding the OI. The field data are collected in a circular-planar configuration. Each probe is controlled through a driver circuit, which biases or unbiases the probes. If a probe is biased, all five p-i-n diodes are "on" or "shorted." If a probe is unbiased, all of its p-i-n diodes are "off" or "opened."

For each field measurement, e.g., the so-called incident-field or the total-field measurement, we collect the scattering parameters (S-parameters) between the transmitter antenna and the nearest collector antenna to the probe via the VNA. For instance, if we want to measure the field at the probe m's location, S_{ji} is measured twice: 1) $S_{ji}^{m,\mathrm{on}}$ when the probe m is shorted and 2) $S_{ji}^{m,\mathrm{off}}$ when the probe is opened. The field at the probe's location is then proportional to the difference

$$\delta S_{ji}^m = S_{ji}^{m,\mathrm{on}} - S_{ji}^{m,\mathrm{off}} \propto E_p^m \qquad (1)$$

where i is the transmitter antenna's index, j is the collector antenna's index, and E_p^m is the electric field along polarization p at the mth probe's location (in this case, ϕ or z). Note that antenna j is the nearest antenna to probe m. In the system presented here, probe m is mounted on the aperture of antenna j, as shown in Fig. 2.

This type of differential measurement suppresses the noise and phase error due to the stress on the cables, the RF multiplexer, and the VNA. That is, because the two measurements (short and open) are performed shortly after each other, the cables remain stationary during the differential data collection and the effect of the cables on the measurement is therefore negligible. The phase error due to different RF routings of the RF multiplexer also vanishes. Thus, the system is no longer sensitive to the cable length, as well as the configuration of the RF multiplexer.

C. Antennas and Probes

The dual-polarized imaging system consists of 12 cavity-backed Vivaldi antennas, distributed evenly on the circumference of a Plexiglas chamber. Each cavity-backed Vivaldi antenna is made from one double-layered Vivaldi antenna (DLVA) and a cylindrical conducting cavity having a diameter of 60.0 mm. Design configuration and radiation characteristics of the DLVA are available in [27]. The DLVA is inserted into

the cylindrical cavity, as shown in Fig. 2(a). For the cavity, we used acrylonitrile butadiene styrene (ABS) plastic pipes partially covered with copper tape, as shown in Fig. 4(b).

There are three main reasons for utilizing cavity-backed Vivaldi antennas, which are: 1) the copper tape shields the antenna from the biasing wire circuitry, and therefore, suppresses unwanted interference from the biasing wires; 2) the radiation pattern of a DLVA, which is not symmetric, becomes symmetric with the inclusion of the circular cavity; and 3) the mutual coupling between antennas is reduced.

Since we are interested in both the TE and TM polarizations, the DLVA (inside the conducting cavity) is mounted at a 45° angle with respect to the longitudinal axis of the chamber, as shown in Fig. 2(a).

In order to measure two polarizations, two probes are required: one in the longitudinal direction and one in the transverse plane. Thus, the two orthogonal probes are each positioned at 45° with respect to the DLVA. The two probes are printed on either side of a substrate, as shown in Fig. 2. The substrate is Arlon DiClad with relative permittivity of 2.5 and thickness of 0.79 mm. Each probe is terminated with a resistor to eliminate RF current in the biasing circuitry. In this configuration, the vertical and horizontal probes measure the E_z (referred to as the TM mode) and E_ϕ (referred to as the TE mode) components, respectively.

We studied the interaction of each probe with their collector antenna using a full simulation of the probe antenna. We combined the finite-element method (FEM) using the Ansys HFSS package and a circuit solver using the Ansys Designer package [28] to simulate each probe. A similar study was performed for the single-polarized system [21]. The equivalent circuits of our p-i-n diodes reported in [21] for both short and open cases were used in the new simulations. In the short case, the p-i-n diode is equivalent to a series resistor and an inductor, which are 0.5 Ω and 0.6 nH, respectively. In the open case, the p-i-n diode equivalent circuit is an inductor in series with a parallel combination of a resistor and capacitor with values of 0.6 nH, 4.0 kΩ, and 71.8 fF. Based on these values, a single cavity-backed Vivaldi antenna with its two probes was fully simulated in the following three scenarios.

(A) The TM probe is shorted and the TE probe is opened.
(B) The TM probe is opened and the TE probe is shorted.
(C) The TM probe is opened and the TE probe is opened.

Using the differential reflection coefficient equation (1) and simulations (A) and (C), $\delta S_{11}^{\mathrm{TM}}$ for the antenna was calculated. Similarly, from simulations (B) and (C), $\delta S_{11}^{\mathrm{TE}}$ was calculated. Here, $\delta S_{11}^{\mathrm{TM}}$ and $\delta S_{11}^{\mathrm{TE}}$ are the differential reflection coefficients for the TM and TE probes, respectively. These results are shown in Fig. 3. As shown in this figure, the antenna is very sensitive to each probe, and the reflection coefficient changes significantly when one of the probes is shorted. Moreover, the two probes operate identically. From Fig. 3(b), it can be observed that $\delta S_{11}^{\mathrm{TM}}$ and $\delta S_{11}^{\mathrm{TE}}$ values are the same, which means the collector antenna does not favor one polarization over the other.

The probe–collector interaction, presented in Fig. 3, is essential in designing such a system. If the interactions of different polarizations are not similar, the imaging system may favor one polarization over the other.
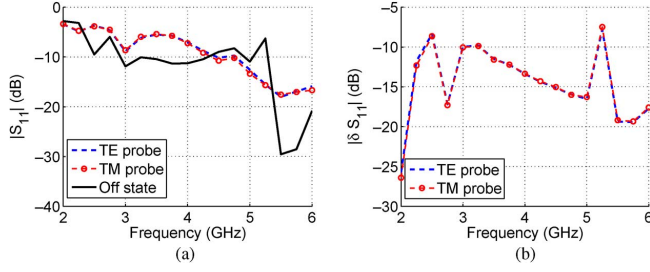
Fig. 3. (a) Comparing the reflection coefficient of the antenna in three cases: both the probes are opened, only the TM probe is shorted, only the TE probe is shorted. (b) Comparing the antenna's differential reflection coefficient of each probe.
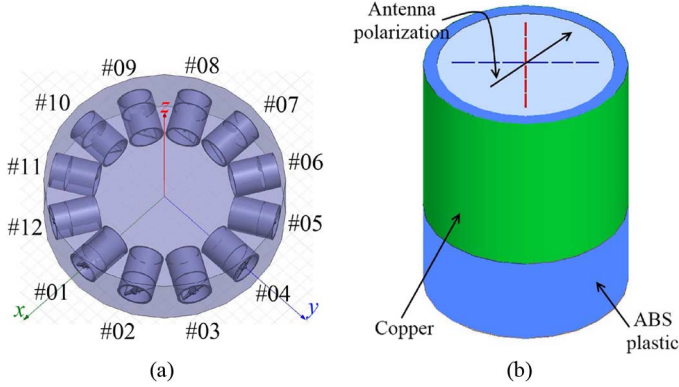

Fig. 4. (a) Simulation configuration of the imaging system comprising 12 antennas. (b) Antenna and its corresponding probes.

D. Full-Wave Simulation of the System

In order to study the illumination field intensity produced in each polarization, we simulated the full imaging system using the Ansys HFSS package [28], which is based on the FEM. The simulation configuration of the imaging system is shown in Fig. 4(a). The antenna's polarization compared to the probes' direction is illustrated in Fig. 4(b).

The imaging domain is a centered square on the x–y plane whose edge length is 13.0 cm. Fig. 5(a) and (b) shows the amplitude and phase of the E_z field polarization (corresponding to the TM mode). Fig. 5(c) and (d) shows the amplitude and phase of ηH_z component, where η is the intrinsic impedance of the background medium (corresponding to the TE mode). These simulations illustrate the presence of the both polarizations inside the imaging domain with the field intensity in the TE and TM polarizations within the same ranges. This is important because the OI should be illuminated with TE- and TM-polarized fields of the same intensity, to prevent the system from favoring one polarization over the other.

III. CALIBRATION

The task of calibrating an imaging system is highly dependent on the system configuration. Several calibration techniques have been reported in the literature, e.g., using the incident-field, or using the scattered-field of a known reference object, such as a perfect electric conductor (PEC). We have studied previously four different combinations of the incident/scattered-field calibration techniques, where the calibration coefficients were either calculated using an analytical approach or obtained from
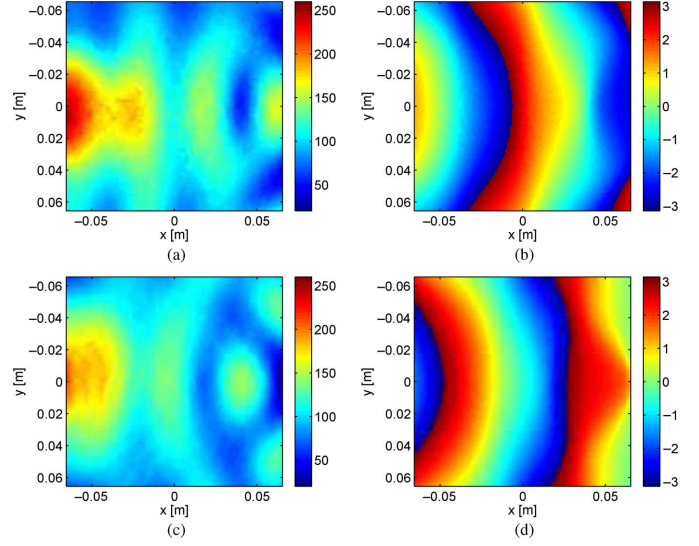

Fig. 5. Simulated field distribution at 4 GHz inside the imaging domain $\mathcal{D}$ [see Fig. 1(b)]. (a) E_z amplitude. (b) E_z phase. (c) ηH_z amplitude. (d) ηH_z phase.

a full-wave simulation of the imaging system. It was shown that utilizing the scattered-field calibration from a PEC cylinder, when illuminated by a line-source model, provides the most suitable calibration method for an MWI system consisting only of the DLVAs [16] and is therefore the method chosen for this system. Each polarization must be calibrated separately for the chosen source models, and this procedure is now discussed.

A. TM Mode

The TM mode in our system is represented by a single longitudinal electric field polarization, parallel to the measurement chamber's axis, which is the E_z component. The TM-mode calibration coefficient is denoted by $C_{\mathcal{F}}^{\mathrm{TM}}$. For each active transmitter t, $C_{\mathcal{F}}^{\mathrm{TM}}$ is calculated at the probe locations as

$$C_{\mathcal{F},t}^{\mathrm{TM}} = \frac{E_{z,t}^{\mathrm{sct\text{-}ref,analytic}}}{E_{z,t}^{\mathrm{sct\text{-}ref,meas}}} \quad (2)$$

where $E_{z,t}^{\mathrm{sct\text{-}ref,meas}}$ is the MST-based measured scattered-field due to the reference PEC cylinder at the TM-probe locations and $E_{z,t}^{\mathrm{sct\text{-}ref,analytic}}$ is the analytically derived scattered field for the same reference PEC cylinder in the presence of an electric line source at the transmitter's location t.

The analytic incident field of an electric line source is denoted by $E_z^{\mathrm{inc,analytic}}$ and is calculated as

$$E_z^{\mathrm{inc,analytic}}(\vec{r}) = \frac{1}{4j} H_0^{(2)}\left(k_b|\vec{r} - \vec{r}_t|\right) \quad (3)$$

where $H_0^{(2)}$ is the zeroth-order Hankel function of the second kind, k_b is the background wavenumber, and $\vec{r}$ and $\vec{r}_t$ represent the observation point and the source point position vectors, respectively. From (3), the scattered field due to a PEC cylinder is calculated analytically as [29]

$$E_{z,t}^{\mathrm{sct,analytical}}(\vec{r}) = \sum_{n=-\infty}^{n=+\infty} \frac{-1}{4j} J_n(k_b a) \frac{H_n^{(2)}(k_b r_t)}{H_n^{(2)}(k_b a)}$$
$$\times e^{jn(\phi - \phi_t)} H_n^{(2)}(k_0 r) \quad (4)$$

where J_n is the Bessel function of the first kind, a is the PEC cylinder's radius, and (r, ϕ), (r_t, ϕ_t) are the cylindrical coordinates of position vectors $\vec{r}, \vec{r}_t$. The scattered field in (4) is calculated for each transmitter. The TM-mode calibration factors, $C_{\mathcal{F}}^{\mathrm{TM}}$, for all probes are stored in a matrix $\underline{C}_{\mathcal{F}}^{\mathrm{TM}}$ with the size of $T \times R_{\mathrm{TM}}$, where T is the total number of transmitters and R_{TM} is the total number of TM-probe receivers. In the system shown in Fig. 1, $T = 12$ and $R_{\mathrm{TM}} = 11$. Thus, the size of $\underline{C}_{\mathcal{F}}^{\mathrm{TM}}$ is 132.

For each OI, the calibrated measured scattered-field data of the TM mode is denoted by $\vec{E}_{\mathrm{TM}}^{\mathrm{sct,meas}}$ and is obtained from

$$\vec{E}_{\mathrm{TM}}^{\mathrm{sct,meas}} = E_z^{\mathrm{sct,meas}} \hat{z} = \underline{C}_{\mathcal{F}}^{\mathrm{TM}} \odot \underline{E}_z^{\mathrm{sct\_meas\_uncal}} \quad (5)$$

where $\underline{E}_z^{\mathrm{sct\_meas\_uncal}}$ is the $T \times R_{\mathrm{TM}}$ matrix containing the MST-based measured scattered field of the z-polarized field for each transmitter and $\odot$ represents the element-wise product between two matrices of the same size.

B. TE Mode

The TE mode in our system represents the TE field polarization with respect to the measurement chamber's imaging plane. This consists of the E_ϕ and E_r components. The TE mode calibration coefficient is denoted by $C_{\mathcal{F}}^{\mathrm{TE}}$. For each active transmitter t, $C_{\mathcal{F}}^{\mathrm{TE}}$ is calculated in a similar fashion as the TM-mode calibration coefficient. Since the TE probes are parallel to the ϕ-axis, the system can only measure the E_ϕ component. The TE calibration coefficients are given as

$$C_{\mathcal{F},t}^{\mathrm{TE}} = \frac{E_{\phi,t}^{\mathrm{sct-ref,analytic}}}{E_{\phi,t}^{\mathrm{sct-ref,meas}}} \quad (6)$$

where $E_{\phi,t}^{\mathrm{sct-ref,meas}}$ is the MST-based measured scattered field by the reference PEC cylinder at the receiver TE-probe locations and the $E_{\phi,t}^{\mathrm{sct-ref,analytic}}$ is the analytic scattered field for the same PEC cylinder in the presence of a magnetic line source at the transmitter location t.

The analytic scattered field, $E_{\phi,t}^{\mathrm{sct-ref,analytic}}$, due to a PEC cylinder of radius a radiated by a magnetic line source is given as

$$E_{\phi,t}^{\mathrm{sct,analytic}}(\vec{r}) = \frac{-1}{4\omega\epsilon_b} \sum_{n=-\infty}^{n=+\infty} \left(H_n^{(2)}(k_b r_t) \frac{J_n'(k_b a)}{H_n^{(2)'}(k_b a)} \right) \times \frac{\partial H_n^{(2)}(k_b r)}{\partial r}. \quad (7)$$

Here, ω is the angular frequency of operation and ϵ_b is the background medium permittivity.

Similar to the TM mode, the calibrated scattered field of the TE mode is calculated as

$$\vec{E}_{\mathrm{TE}}^{\mathrm{sct,meas}} = E_\phi^{\mathrm{sct,meas}} \hat{\phi} = \underline{C}_{\mathcal{F}}^{\mathrm{TE}} \odot \underline{E}_\phi^{\mathrm{sct\_meas\_uncal}} \quad (8)$$

where $\underline{E}_\phi^{\mathrm{sct\_meas\_uncal}}$ is the matrix containing MST-based measured ϕ-polarized scattered fields.

C. Calibration Results

For our system, we utilize a PEC cylinder with a diameter of 3.5 in as the calibration reference object. Similar to the single-polarized system in [21], we compared the analytical and measured fields scattered by the calibration object. Fig. 6 shows the
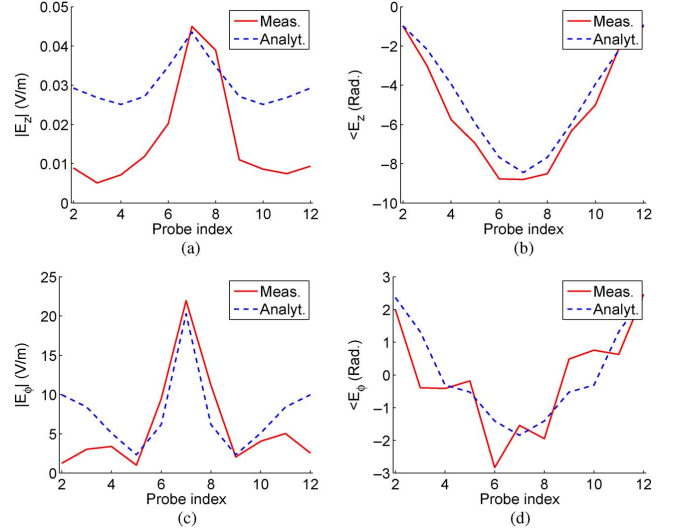

Fig. 6. Comparison of scattered field by the PEC cylinder from measurement and analytical solution at 4.3 GHz. (a) TM probe amplitude. (b) TM probe phase. (c) TE probe amplitude. (d) TE probe phase.

comparison. Fig. 6(a) and (b) compares the amplitude and phase of the scattered E_z field for the TM mode. Fig. 6(c) and (d) compares the amplitude and phase of the scattered E_ϕ field for the TE mode. In the numerical image reconstruction, the antennas and the imaging system are not fully modeled, thus there is a mismatch between the measured and analytical solutions presented in Fig. 6. However, note that the frequencies where there is better matching between the results (such as at 4.3 GHz) are selected for better image reconstruction (see Section V and [30]).

IV. INVERSION ALGORITHM

For the inverse problem, we consider the OI confined within an imaging domain $\mathcal{D}$, as shown in Fig. 1(b), surrounded by transmitters and receivers co-located on a measurement surface $\mathcal{S}$. The imaging domain is immersed in a homogeneous background medium with a known complex relative permittivity, ϵ_b. The contrast of the OI is defined as

$$\chi(\vec{r}) = \frac{(\epsilon_r(\vec{r}) - \epsilon_b)}{\epsilon_b} \quad (9)$$

where $\epsilon_r(\vec{r})$ is the complex relative permittivity of the OI. Outside the imaging domain, $\mathcal{D}$, $\chi = 0$. Here, the background and OI are assumed nonmagnetic, i.e., their relative permeability $\mu_r = 1$.

The calibrated TE- and TM-polarized data are inverted using the contrast source inversion (CSI) algorithm [31] formulated using the FEM [8], [32]. The CSI method formulates the optimization problem in terms of two variables: the contrast, χ, and the contrast source, $\vec{w}_t$, which is defined as

$$\vec{w}_t \triangleq \chi \vec{E}^{\mathrm{tot}}. \quad (10)$$

The CSI cost functional written with respect to these variables is given as

$$\mathcal{C}^{\mathrm{CSI}}(\chi, \vec{w}_t) = \mathcal{C}^{\mathcal{S}}(\vec{w}_t) + \mathcal{C}^{\mathcal{D}}(\chi, \vec{w}_t) \quad (11)$$

where the data-error formula $\mathcal{C}^{\mathcal{S}}(\vec{w}_t)$ and the domain-error formula $\mathcal{C}^{\mathcal{D}}(\chi, \vec{w}_t)$ are given by

$$\mathcal{C}^{\mathcal{S}}(\vec{w}_t)$$
$$= \frac{\sum_t \left\| \vec{E}_t^{\text{sct,meas}}(\vec{r}) - \mathcal{G}_{\mathcal{S}}\{\vec{w}_t\} \right\|_{\mathcal{S}}^2}{\sum_t \| \vec{u}_t(\vec{r}) \|_{\mathcal{S}}^2}$$
$$\mathcal{C}^{\mathcal{D}}(\chi, \vec{w}_t)$$
$$= \frac{\sum_t \left\| \chi(\vec{r})\vec{E}_t^{\text{inc}}(\vec{r}) - \vec{w}_t(\vec{r}) + \chi(\vec{r})\mathcal{G}_{\mathcal{D}}\{\vec{w}_t\} \right\|_{\mathcal{D}}^2}{\sum_t \left\| \chi(\vec{r})\vec{E}_t^{\text{inc}}(\vec{r}) \right\|_{\mathcal{D}}^2}. \quad (12)$$

For a transmitter t, $\vec{E}_t^{\text{sct,meas}}$ is the calibrated measured scattered field at the receiver locations on surface $\mathcal{S}$, while $\vec{E}_t^{\text{inc}}$ is the analytic incident field within the imaging domain $\mathcal{D}$. In the data-error formula, $\mathcal{G}_{\mathcal{S}}$ is an operator that returns the scattered field on a measurement surface $\mathcal{S}$ given the contrast source variable $\vec{w}_t$. For the domain-error formula, $\mathcal{G}_{\mathcal{D}}$ is an operator that returns the scattered field in the imaging domain $\mathcal{D}$ from the contrast source variables $\vec{w}_t$. Both these operators depend on the background medium and the assumed polarization for the problem. Furthermore, the operators are independent of the transmitter location and the contrast values, thus they are formed once in the CSI algorithm and recalled when necessary.

For the TM problem, the vectors in the CSI functional have only one spatial component polarized along the z-axis

$$\vec{w}_t(\vec{r}) = w_{t,z}(\vec{r})\hat{z}$$
$$\vec{E}_t^{\text{sct,meas}}(\vec{r}) = E_{t,z}^{\text{sct,meas}}(\vec{r})\hat{z}$$
$$\vec{E}_t^{\text{inc}}(\vec{r}) = E_{t,z}^{\text{inc}}(\vec{r})\hat{z}. \quad (13)$$

In the TE case, the measured field vector has only a single spatial component along the ϕ-axis, i.e.,

$$\vec{E}_t^{\text{sct,meas}}(\vec{r}) = E_{t,\phi}^{\text{sct,meas}}(\vec{r})\hat{\phi}$$

whereas the contrast source and incident field vectors have transverse field components

$$\vec{w}_t(\vec{r}) = w_{t,x}(\vec{r})\hat{x} + w_{t,y}(\vec{r})\hat{y}$$
$$\vec{E}_t^{\text{inc}}(\vec{r}) = E_{t,x}^{\text{inc}}(\vec{r})\hat{x} + E_{t,y}^{\text{inc}}(\vec{r})\hat{y}. \quad (14)$$

For either polarizations, the CSI algorithm first updates the contrast source variables by a conjugate-gradient method with the Polak–Ribière search direction and then it updates the contrast variables analytically [31]. The outcome of the inversion algorithm is enhanced by utilizing a multiplicative regularizer [33], [34]. This regularizer offers edge-preserving capabilities, as well as the ability to suppress noise in the measurement data [35].

V. IMAGING RESULTS

Using the proposed dual-polarized imaging system and the multiplicatively regularized FEM-CSI algorithm, we reconstructed the electrical properties of four different OIs, which are depicted in Fig. 7. The relative permittivity of the nylon cylinder and the wooden cuboid, shown in Fig. 7, are
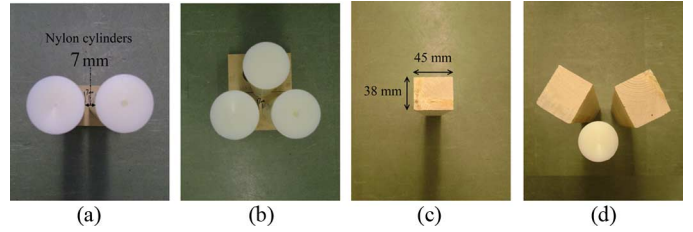

Fig. 7. Photographs of dielectric objects used for imaging. (a) Resolution test, which consists of two nylon cylinders separated by 7 mm. (b) Three nylon cylinders separated by 7 mm. (c) Wooden cuboid. (d) Two wooden cuboids and a nylon cylinder.

$\epsilon_r^{\text{nylon}} = 2.7 - j0.03$, and $\epsilon_r^{\text{wood}} = 1.9 - j0.1$ (as measured using the Agilent 85070E dielectric probe kit). The circular cross section of the nylon cylinders has a diameter of 38.1 mm. The average edge length of the wooden cuboids cross section is 40 mm. Due to the limited size of the collected dataset ($12 \times 11 = 132$ data points per polarization), more complicated targets will be difficult to reconstruct successfully because of the nonlinear property of the inverse scattering problem associated with MWI [22].

For each OI, the MST-based TE and TM data were collected with the objects placed in the center of the measurement chamber. For each polarization, data were gathered in the frequency range of 3–5 GHz in steps of 0.1 GHz. The measurement frequency range was selected based on the antenna's operational frequency (higher than 3 GHz) and the mismatch between the measured and analytical solution of the calibration object (see Section III).

The data at several discrete frequencies were inverted simultaneously using the CSI algorithm; here we assumed that the dielectric properties of the OIs are frequency invariant. For the TE case, the frequencies utilized were

$$\{3.9, 4.0, 4.1, 4.2, 4.3, 4.4, 4.8, 4.9, \text{ and } 5.0\} \text{ GHz.}$$

In the TM mode, the frequencies used were

$$\{3.5, 3.6, 3.7, 3.8, 4.1, 4.2, 4.3, 4.9, \text{ and } 5.0\} \text{ GHz.}$$

The frequencies for each mode were selected based on how well the measured scattered fields for the PEC reference object compare to the analytic fields. For instance, at 4.3 GHz, the measured scattered field by the PEC cylinder matches the analytical solution for the both polarizations, as shown in Fig. 6.

The inversion results of the two-nylon cylinders [see Fig. 7(a)], three-nylon cylinders [see Fig. 7(b)], the wooden cuboid [see Fig. 7(c)], and two-wooden cuboids with the cylinder [see Fig. 7(d)] are shown in Figs. 8–11, respectively.

VI. DISCUSSION

MWI systems have been investigated for decades. Most research has focused on the improvement of imaging algorithms. Although the imaging algorithms are fundamentally important, implementing novel experimental systems is also eminently important. With regard to experimental microwave systems, collecting different field polarizations requires a sophisticated design that can be feasibly implemented. In the past, all compact MWI systems have implemented a single polarization. In this
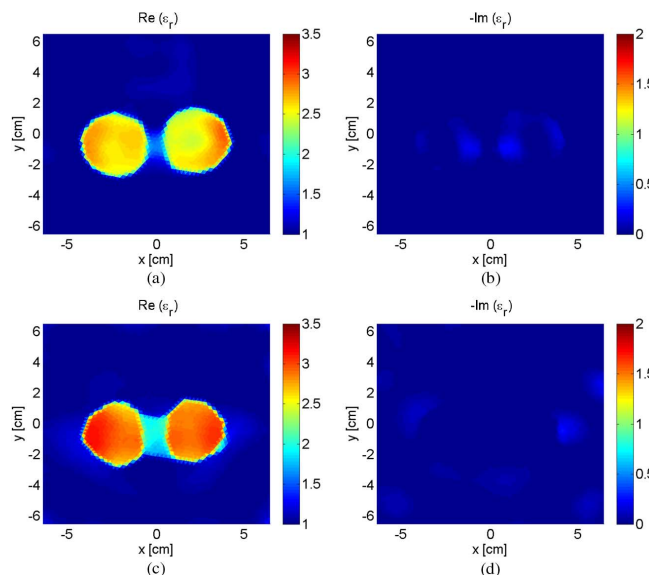
Fig. 8. Reconstructed real (*left*) and imaginary (*right*) parts of relative permittivity of the two-nylon object. (a) and (b) Presents the TE-mode inversion. (c) and (d) Presents the TM-mode inversion.
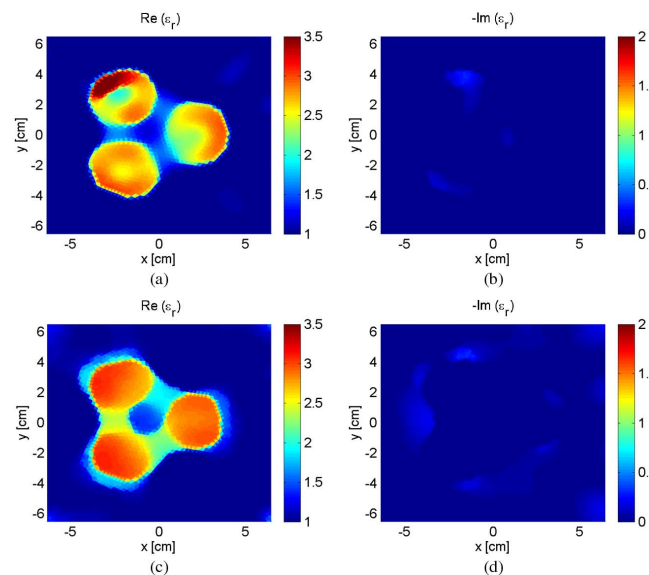

Fig. 9. Reconstructed real (*left*) and imaginary (*right*) parts of relative permittivity of the three-nylon object. (a) and (b) Presents the TE-mode inversion. (c) and (d) Presents the TM-mode inversion.
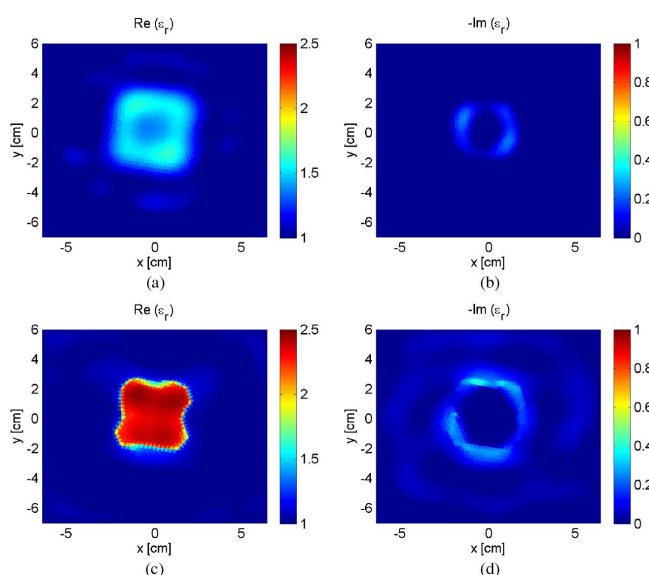

Fig. 10. Reconstructed real (*left*) and imaginary (*right*) parts of relative permittivity of the wooden cuboid object. (a) and (b) Presents the TE-mode inversion. (c) and (d) Presents the TM-mode inversion.
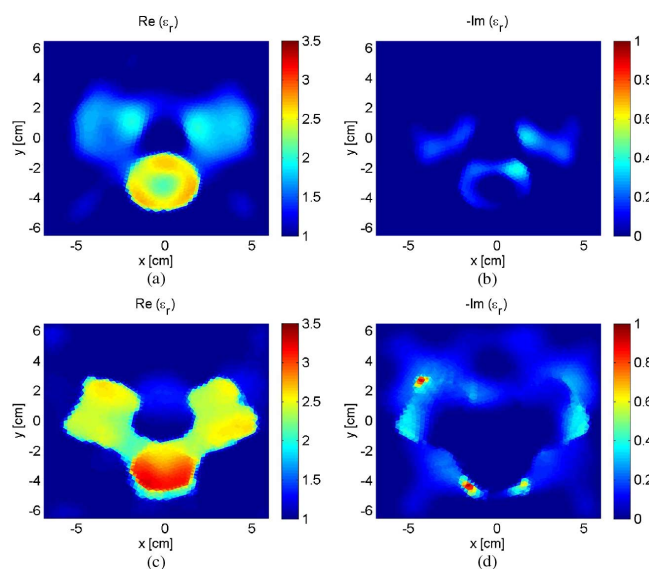

Fig. 11. Reconstructed real (*left*) and imaginary (*right*) parts of relative permittivity of two-wooden cuboids with the cylinder object. (a) and (b) Presents the TE-mode inversion. (c) and (d) Presents the TM-mode inversion.

paper, we have introduced a new MWI system, which implements, in relatively easy way, data collection in two polarizations using scattering probes.

The use of scattering probes provides several important advantages for an MWI system, which are: 1) the field measurement is handled through modulating the probes or the differential measurement technique described in this paper; 2) MST-based measurements collect differential measurements in a short period of time; thus, it has the potential to reduce many sources of experimental error; 3) inactive probes are minimal scatterers, thus the mutual coupling between the probes is very low and the number of measurement points can be increased significantly especially in a near-field MWI system; and 4) probes can be aligned with different polarizations, making multipolarized data collection a possibility.

In the dual-polarized prototype system presented here, we only utilized 12 antennas and 24 probes; 12 probes were used per polarization. The imaging results obtained from the dielectric objects, even with a limited-size dataset, show that the TM and TE datasets provide different information. This is consistent with previous synthetic-data studies on TE and TM image reconstruction that show the two polarizations provide a different amount of information particularly in the near-field region of the antennas [36]. As shown in Figs. 8–11, the TE dataset provides a higher resolution, i.e., the objects are clearly distinguishable from each other. However, in the TE mode, the reconstructed dielectric values are lower than the expected permittivities and the permittivity distribution is nonuniform. On the other hand, the TM-mode data provide a more uniform image of the object's

interior with the permittivity closer to the expected value. Compared to the TE mode, the resolution of the TM-mode data is worse; the separation between the objects is not clear.

Having such a dual-polarized system allows us to investigate several issues regarding the imaging quality achievable with MWI. For example, in future work, we plan on combining the TM and TE datasets to study whether image quality, resolution, and accuracy can be further improved over images obtained using a single polarization. Such a combination of polarizations can be performed in different ways, such as using one polarization as the initial guess for the other polarization or simultaneous polarization inversion, but these novel approaches are not within the scope of this paper.

VII. CONCLUSION

In this work, we have reported on a novel technique that allows MWI using multiple polarizations. We have achieved two polarizations within the same system (TE and TM). We also presented a calibration procedure for the TM and TE polarized data, sufficient for obtaining 2-D tomographic images. The groundwork has been laid for our future work, which is the application of this technique, in suitably modified form, to the building of fully 3-D vectorial MWI systems.

ACKNOWLEDGMENT

REFERENCES

[1] M. Ghasr, M. Abou-Khousa, S. Kharkovsky, R. Zoughi, and D. Pommerenke, "Portable real-time microwave camera at 24 GHz," *IEEE Trans. Antennas Propag.*, vol. 60, no. 2, pp. 1114–1125, Feb. 2012.

[2] A. Abubakar and P. Van Den Berg, "nonlinear three-dimensional inversion of cross-well electrical measurements," *Geophys. Prospect.*, vol. 48, no. 1, pp. 109–134, 2000.

[3] N. Nikolova, "Microwave imaging for breast cancer," *IEEE Microw. Mag.*, vol. 12, no. 7, pp. 78–94, Dec. 2011.

[4] J. Geffrin and P. Sabouroux, "Continuing with the Fresnel database: Experimental setup and improvements in 3-D scattering measurements," *Inverse Problems*, vol. 25, 2009, Art. ID 024001.

[5] C. Gilmore, A. Zakaria, P. Mojabi, M. Ostadrahimi, S. Pistorius, and J. Lo Vetri, "The University of Manitoba microwave imaging repository: A two-dimensional microwave scattering database for testing inversion and calibration algorithms," *IEEE Antennas Propag. Mag.*, vol. 53, no. 5, pp. 126–133, Oct. 2011.

[6] Q. Fang, P. Meaney, and K. Paulsen, "Viable three-dimensional medical microwave tomography: Theory and numerical experiments," *IEEE Trans. Antennas Propag.*, vol. 58, no. 2, pp. 449–458, Feb. 2010.

[7] J. De Zaeytijd, A. Franchois, C. Eyraud, and J. Geffrin, "Full-wave three-dimensional microwave imaging with a regularized Gauss–Newton method-theory and experiment," *IEEE Trans. Antennas Propag.*, vol. 55, no. 11, pp. 3279–3292, Nov. 2007.

[8] A. Zakaria, C. Gilmore, and J. LoVetri, "Finite-element contrast source inversion method for microwave imaging," *Inverse Problems*, vol. 26, 2010, Art. ID 115010.

[9] P. Mojabi and J. LoVetri, "Microwave biomedical imaging using the multiplicative regularized Gauss–Newton inversion," *IEEE Antennas Wireless Propag. Lett.*, vol. 8, pp. 645–648, 2009.

[10] M. Klemm, I. Craddock, J. Leendertz, A. Preece, and R. Benjamin, "Radar-based breast cancer detection using a hemispherical antenna array-experimental results," *IEEE Trans. Antennas Propag.*, vol. 57, no. 6, pp. 1692–1704, Jun. 2009.

[11] A. Franchois, A. Joisel, C. Pichot, and J. Bolomey, "Quantitative microwave imaging with a 2.45-GHz planar microwave camera," *IEEE Trans. Med. Imag.*, vol. 17, no. 4, pp. 550–561, Aug. 1998.

[12] L. Crocco and A. Litman, "On embedded microwave imaging systems: Retrievable information and design guidelines," *Inverse Problems*, vol. 25, 2009, Art. ID 065001.

[13] J. Stang, M. Haynes, P. Carson, and M. Moghaddam, "A preclinical system prototype for focused microwave thermal therapy of the breast," *IEEE Trans. Biomed. Eng.*, vol. 59, no. 9, pp. 2431–2438, Sep. 2012.

[14] S. Semenov, J. Kellam, Y. Sizov, A. Nazarov, T. Williams, B. Nair, A. Pavlovsky, V. Posukh, and M. Quinn, "Microwave tomography of extremities: 1. Dedicated 2-D system and physiological signatures," *Phys. Med. Biol.*, vol. 56, pp. 2005–2017, 2011.

[15] P. Meaney, M. Fanning, T. Raynolds, C. Fox, Q. Fang, C. Kogel, S. Poplack, and K. Paulsen, "Initial clinical experience with microwave breast imaging in women with normal mammography," *Acad. Radiol.*, vol. 14, no. 2, pp. 207–218, 2007.

[16] M. Ostadrahimi, P. Mojabi, C. Gilmore, A. Zakaria, S. Noghanian, S. Pistorius, and J. LoVetri, "Analysis of incident field modeling and incident/scattered field calibration techniques in microwave tomography," *IEEE Antennas Wireless Propag. Lett.*, vol. 10, pp. 900–903, 2011.

[17] T. Henriksson, N. Joachimowicz, C. Conessa, and J. Bolomey, "Quantitative microwave imaging for breast cancer detection using a planar 2.45 GHz system," *IEEE Trans. Instrum. Meas.*, vol. 59, no. 10, pp. 2691–2699, Oct. 2010.

[18] J. Geffrin, P. Sabouroux, and C. Eyraud, "Free space experimental scattering database continuation: Experimental setup and measurement precision," *Inverse Problems*, vol. 21, pp. S117–S130, 2005.

[19] S. Kharkovsky, A. Ryley, V. Stephen, and R. Zoughi, "Dual-polarized near-field microwave reflectometer for noninvasive inspection of carbon fiber reinforced polymer-strengthened structures," *IEEE Trans. Instrum. Meas.*, vol. 57, no. 1, pp. 168–175, Jan. 2008.

[20] J. Bolomey and F. Gardiol, *Engineering Applications of the Modulated Scatterer Technique.* Norwood, MA: Artech House, 2001.

[21] M. Ostadrahimi, P. Mojabi, S. Noghanian, L. Shafai, S. Pistorius, and J. LoVetri, "A novel microwave tomography system based on the scattering probe technique," *IEEE Trans. Instrum. Meas.*, vol. 61, no. 2, pp. 379–390, Feb. 2012.

[22] M. Ostadrahimi, P. Mojabi, S. Noghanian, J. LoVetri, and L. Shafai, "A multiprobe-per-collector modulated scatterer technique for microwave tomography," *IEEE Antennas Wireless Propag. Lett.*, vol. 10, pp. 1445–1448, 2011.

[23] J. Richmond, "A modulated scattering technique for measurement of field distributions," *IRE Trans. Microw. Theory Techn.*, vol. MTT-3, no. 4, pp. 13–15, Apr. 1955.

[24] H. Memarzadeh-Tehran, J. Laurin, and R. Kashyap, "Optically modulated probe for precision near-field measurements," *IEEE Trans. Instrum. Meas.*, vol. 59, no. 10, pp. 2755–2762, Oct. 2010.

[25] M. Abou-Khousa, M. Ghasr, S. Kharkovsky, D. Pommerenke, and R. Zoughi, "Modulated elliptical slot antenna for electric field mapping and microwave imaging," *IEEE Trans. Antennas Propag.*, vol. 59, no. 3, pp. 733–741, Mar. 2011.

[26] A. Cullen and J. Parr, "A new perturbation method for measuring microwave fields in free space," *Proc. Inst. Elect. Eng.—Radio Electron. Eng.*, vol. 102, no. 6, pt. B, pp. 836–844, 1955.

[27] M. Ostadrahimi, S. Noghanian, L. Shafai, A. Zakaria, C. Kaye, and J. LoVetri, "Investigating a double layer Vivaldi antenna design for fixed array field measurement," *Int. J. Ultra Wideband Commun. Syst.*, vol. 1, no. 4, pp. 282–290, 2010.

[28] HFSS Simulator Package. Ansys, Canonsburg, PA, 2012. [Online]. Available: www.ansys.com

[29] C. A. Balanis, *Advanced Engineering Electromagnetics*. New York: Wiley, 1989.

[30] C. Gilmore, P. Mojabi, A. Zakaria, M. Ostadrahimi, C. Kaye, S. Noghanian, L. Shafai, S. Pistorius, and J. LoVetri, "A wideband microwave tomography system with a novel frequency selection procedure," *IEEE Trans. Biomed. Eng.*, vol. 57, no. 4, pp. 894–904, Apr. 2010.

[31] P. Van Den Berg and R. Kleinman, "A contrast source inversion method," *Inverse Problems*, vol. 13, pp. 1607–1620, 1997.

[32] A. Zakaria and J. LoVetri, "The finite-element method contrast source inversion algorithm for 2-D transverse electric vectorial problems," *IEEE Trans. Antennas Propag.*, vol. 60, no. 10, pp. 4757–4765, Oct. 2012.

[33] A. Zakaria and J. LoVetri, "Application of multiplicative regularization to the finite-element contrast source inversion method," *IEEE Trans. Antennas Propag.*, vol. 59, no. 9, pp. 3495–3498, Sep. 2011.

[34] A. Abubakar, P. Van den Berg, and J. Mallorqui, "Imaging of biomedical data using a multiplicative regularized contrast source inversion method," *IEEE Trans. Microw. Theory Techn.*, vol. 50, no. 7, pp. 1761–1771, Jul. 2002.

[35] P. M. van den Berg, A. Abubakar, and J. Fokkema, "Multiplicative regularization for contrast profile inversion," *Radio Sci.*, vol. 38, no. 2, pp. 23(1)–23(10), 2003.

[36] P. Mojabi and J. LoVetri, "Comparison of TE and TM inversions in the framework of the Gauss–Newton method," *IEEE Trans. Antennas Propag.*, vol. 58, no. 4, pp. 1336–1348, Apr. 2010.

Majid Ostadrahimi (S'09–M'12) received the B.Sc. and M.Sc. degrees (with highest distinction) in electrical engineering from the Sharif University of Technology and Iran University of Science and Technology, Tehran, Iran, in 2003 and 2006, respectively, and the Ph.D. degree in electrical and computer engineering from the University of Manitoba, Winnipeg, MB, Canada, in 2012.

He is currently a Post-Doctoral Fellow with the Department of Electrical and Computer Engineering, University of Manitoba. His main research interests lie in the areas of near-field measurement, the MST, inverse problems, biomedical imaging, and the design and development of MWI systems.

Dr. Ostadrahimi was the IEEE Winnipeg section treasurer (2010 and 2011).

Amer Zakaria (S'05–M'07) received the B.Sc. degree in electrical engineering (*summa cum laude*) from the American University of Sharjah, Sharjah, U.A.E., in 2005, the M.Sc. degree in microwave engineering (with high distinction) from the Munich University of Technology, Munich, Germany, in 2007, and the Ph.D. degree in electrical engineering from the University of Manitoba, Winnipeg, MB, Canada, in 2012.

In 2006 and 2007, he was with the RF Verification Department, Infineon Technologies, Munich, Germany. He currently is a Postdoctoral Fellow with the Department of Electrical and Computer Engineering, University of Manitoba. His research interests include inverse problems, computational electromagnetics, and the development of MWI systems.

Joe LoVetri (S'84–M'84–SM'09) received the B.Sc. (with distinction) and M.Sc. degrees in electrical engineering from the University of Manitoba, Winnipeg, MB, Canada, in 1984 and 1987, respectively, the Ph.D. degree in electrical engineering from the University of Ottawa, Ottawa, ON, Canada, in 1991, and the M.A. degree in philosophy from the University of Manitoba, Winnipeg, MB, Canada, in 2006.

From 1984 to 1986 he was an Electromagnetic Interference (EMI)/Electromagnetic Compatibility (EMC) Engineer with the Defence Division, Sperry Winnipeg, MB, Canada. From 1986 to 1988, he was a TEMPEST Engineer with the Communications Security Establishment, Ottawa, ON, Canada. From 1988 to 1991, he was a Research Officer with the Institute for Information Technology, National Research Council of Canada. His academic career began in 1991, when he joined the Department of Electrical and Computer Engineering, The University of Western Ontario, where he remained until 1999. From 1997 to 1998, he spent a sabbatical year with the TNO Physics and Electronics Laboratory, The Hague, The Netherlands, during which time he was involved with time-domain computational methods and ground penetrating RADAR. In 1999, he joined the University of Manitoba, where he is currently a Professor with the Department of Electrical and Computer Engineering. From 2004 to 2009, he was the Associate Dean (Research and Graduate Programs) for the Faculty of Engineering. His main research interests lie in the areas of time-domain computational electromagnetics, modeling of EMC problems, inverse problems, and biomedical imaging.

Dr. LoVetri has been a Registered Professional Engineer in the Province of Ontario since 1994. He has been Chapter chair for the IEEE EMC Ottawa Chapter, as well as the Winnipeg Waves Chapter (AP/MTT). From 2005 to 2009, he was the national representative for Commission E, Canadian National Committee, URSI. In 2010 he cochaired the Ultrawideband and Short-Pulse Electromagnetics Conference, which was part of AMEREM, Ottawa, ON, Canada, 2010. He was the recipient of the 1993 URSI Young Scientist Award, 2000 IEEE EMC Best Symposium Paper Award, and the 2007 ACES Outstanding Paper Award, the 2002 University of Manitoba Rh Award for Outstanding Contributions to Scholarship and Research in the Applied Sciences.

Lotfollah Shafai (S'67–M'69–SM'75–F'88–LF'07) received the B.Sc. degree from the University of Tehran, Tehran, Iran, in 1963, and the M.Sc. and Ph.D. degrees from the University of Toronto, Toronto, ON, Canada, in 1966 and 1969, respectively.

In November 1969, he joined the Department of Electrical and Computer Engineering, University of Manitoba, Winnipeg, MB, Canada, as a Lecturer, Assistant Professor (1970), Associate Professor (1973), Professor (1979), and Distinguished Professor (2002). His assistance to industry was instrumental in establishing an Industrial Research Chair in Applied Electromagnetics at the University of Manitoba, in 1989, which he held until July 1994.

Dr. Shafai established the Symposium on Antenna Technology and Applied Electromagnetics (ANTEM) at the University of Manitoba, in 1986, which has grown to be the premier Canadian conference in antenna technology and related topics. He is a Life Fellow of The Royal Society of Canada. He holds a Canada Research Chair in Applied Electromagnetics and was the International chair of Commission B, URSI (2005–2008). In 2009 he was elected a Fellow of the Engineering Institute of Canada He has been the recipient of numerous awards. In 1978, his contribution to the design of the first miniaturized satellite terminal for the Hermes satellite was selected as the Meritorious Industrial Design. In 1984, he was the recipient of the Professional Engineers Merit Award, and in 1985, "The Thinker" Award from the Canadian Patents and Development Corporation. From the University of Manitoba, he was the recipient of the Research Award in 1983, 1987, and 1989, the Outreach Award in 1987, and the Sigma Xi Senior Scientist Award in 1989. He was the recipient of the 1990 Maxwell Premium Award of the IEE, U.K., and in 1993 and 1994, the Distinguished Achievement Awards from the Corporate Higher Education Forum. He was the recipient of the 1998 Winnipeg RH Institute Foundation Medal for Excellence in Research. He was the recipient of the 1999 and 2000 University of Manitoba Research Award. He was a recipient of the IEEE Third Millennium Medal in 2000. In 2002, he became a Fellow of The Canadian Academy of Engineering and Distinguished Professor at the University of Manitoba. In 2003, he was the recipient of an IEEE Canada Reginald A. Fessenden Medal for "Outstanding Contributions to Telecommunications and Satellite Communications" and a Natural Sciences and Engineering Research Council (NSERC) Synergy Award for "Development of Advanced Satellite and Wireless Antennas." He was the recipient of IEEE Chen-To-Tai Distinguished Educator Award. He was also the recipient of the 2011 Killam Prize in Engineering from The Canada Council for his "outstanding Canadian career achievements in engineering, and his research on antennas."